Multiple Loop Conformations of Peptides Predicted by Molecular Dynamics Simulations Are Compatible with Nuclear Magnetic Resonance[†]

Heiko Carstens,[‡] Christian Renner,[§] Alexander G. Milbradt,[§] Luis Moroder,[§] and Paul Tavan*,[‡]

Lehrstuhl für BioMolekulare Optik, Oettingenstrasse 67, Ludwig-Maximilians-Universität München, 80538 München, Germany, and Max-Planck-Institut für Biochemie, Am Klopferspitz 18a, 82152 Martinsried, Germany

Received December 6, 2004; Revised Manuscript Received January 25, 2005

ABSTRACT: The affinity and selectivity of protein−protein interactions can be fine-tuned by varying the size, flexibility, and amino acid composition of involved surface loops. As a model for such surface loops, we study the conformational landscape of an octapeptide, whose flexibility is chemically steered by a covalent ring closure integrating an azobenzene dye into and by a disulfide bridge additionally constraining the peptide backbone. Because the covalently integrated azobenzene dyes can be switched by light between a bent cis state and an elongated trans state, six cyclic peptide models of strongly different flexibilities are obtained. The conformational states of these peptide models are sampled by NMR and by unconstrained molecular dynamics (MD) simulations. Prototypical conformations and the free-energy landscapes in the high-dimensional space spanned by the ϕ/ψ angles at the peptide backbone are obtained by clustering techniques from the MD trajectories. Multiple open-loop conformations are shown to be predicted by MD particularly in the very flexible cases and are shown to comply with the NMR data despite the fact that such open-loop conformations are missing in the refined NMR structures.

Protein−ligand as well as protein−protein interactions are highly regulated processes. The affinity and selectivity of these interactions are frequently fine-tuned by variations in the size, flexibility, and amino acid composition of involved surface loops (*1*−*4*). In such cases, the folding pattern of the protein solely serves as a structural scaffold for the loops, which represent the active site and mediate the function. Therefore, the conformational properties of semiflexible or flexible surface loops have attracted considerable attention (*5*−*7*).

Mobile parts of proteins, such as surface loops, frequently escape observation in X-ray crystallography or even preclude crystallization at all. Here, NMR spectroscopy is the experimental method of choice for structural investigations (*8*). However, the averaging of loop conformations on the NMR time scale of seconds complicates the interpretation of the experimentally derived constraints, because the usual NMR refinement protocols generally assume the prevalence of a single loop conformation (*9*−*18*).

In principle, an atomistic picture of the protein conformational dynamics is accessible by computer simulations, provided that the applied theoretical model is sufficiently accurate and the available computing power allows the accumulation of statistically significant data. Here, despite various well-known insufficiencies of the available molecular mechanics (MM)[1] force fields (*19*, *20*), corresponding molecular dynamics (MD) simulations (*21*−*23*) currently represent the standard and MM−MD simulations are frequently employed to generate equilibrium conformational ensembles of biomolecules.

Comparisons with the nuclear Overhauser effect (NOE) distance restraints derived from NMR experiments can be based on such ensembles (*18*, *24*−*27*). Studies of this kind concerning peptides (*18*), flexible β peptides (*24*, *25*), proteins (*26*, *28*, *29*), and DNA (*27*) have shown good agreement with the experimental data. In MD simulations of the β-sheet peptide betanova (*30*), different peptide conformations were found to satisfy different subsets of the NOEs in a way that the total ensemble of conformations fulfills the whole set of experimental constraints. The ability of MD simulations to complement NMR data of small and flexible molecules became also apparent in a study of the RGDW peptide (*31*) and in the work of Lee and Kollman (*32*), who pointed out that the usual approximate treatment of the solvent during NMR structure refinements leads to unreliable structures. Hence, it was suggested to complement the NMR refinement procedure by MD simulations with an explicit solvent model and an accurate treatment of the long-range electrostatics. Further encouraging agreements between NMR experiments and MD simulations were found for the internal dynamics of proteins as monitored by relaxation or order parameters (*33*−*36*).

[†] This work has been funded in part by the Deutsche Forschungsgemeinschaft (SFB 533 C1/A8).

* To whom correspondence should be addressed. E-mail: tavan@physik.uni-muenchen.de. Telephone: 49-89-2180-9220. Fax: 49-89-2180-9202.

[‡] Ludwig-Maximilians-Universität München.

[§] Max-Planck-Institut für Biochemie.

[1] Abbreviations: NMR, nuclear magnetic resonance; MD, molecular dynamics; MM, molecular mechanics; NOE, nuclear Overhauser effect; APB, (4-amino)phenylazobenzoic acid; AMPB, (4-aminomethyl)-phenylazobenzoic acid; DMSO, dimethyl sulfoxide; DG, distance geometry; MD-SA, molecular dynamics-simulated annealing; DFT, density functional theory; FES, free-energy surface; PCA, principal component analysis.

10.1021/bi047453r CCC: $30.25 © 2005 American Chemical Society
Published on Web 02/26/2005

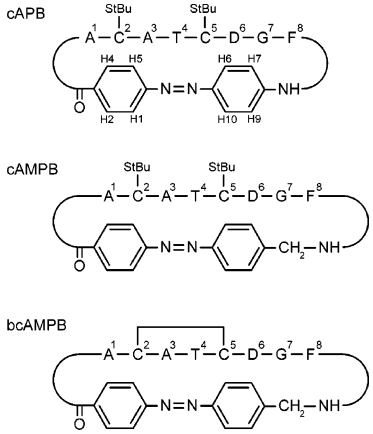

FIGURE 1: Chemical structures of the model peptides. An octapeptide is cyclizised with a derivative of azobenzene.

Because we are specifically interested in flexible peptide loops, thermally sampling several conformational states, we have chosen model systems that are simple enough to be accessed by a combined NMR and MD study. We have recently constructed peptidic systems by backbone cyclization of an octapeptide derived from the thioredoxin reductase with (4-amino)phenylazobenzoic acid (APB) or (4-aminomethyl)phenylazobenzoic acid (AMPB) (*37*) (see Figure 1). While the active-site sequence Ala-Cys-Ala-Thr-Cys-Asp-Gly-Phe adopts a well-defined structure in the native enzyme, namely, the beginning of a 3_{10} helix, in our photoresponsive azopeptides, different conformational preferences depending on the isomeric state of the azobenzene chromophore were observed by NMR (*38*, *39*). The trans isomers showed only a limited flexibility, whereas the cis isomers were characterized by sizable conformational variability. Ultrafast time-resolved spectroscopy in the UV/vis and infrared range revealed a surprisingly complex conformational dynamics considering the small size of the model system (*38*, *40*−*42*). MD simulations were used to characterize the light-induced conformational relaxation dynamics of these peptides on the subnanosecond time scale in detail (*20*, *40*, *43*). The balance between conformational restriction and structural variability apparently leads to a highly complex energy landscape in resemblance to semiflexible bioactive surface loops of proteins, and therefore, the peptides studied here might represent valuable models for the study of conformational heterogeneity and dynamics.

In the present work, we want to show that, in a generally applicable approach, unconstrained MD simulations of the azopeptides in solution, which are based on an MM force field that has not been specifically optimized toward our specific model systems, can reproduce the experimental NMR data. With the use of novel methods for statistical data analysis particularly suited to deal with high-dimensional data spaces, we obtain a detailed picture of multiple thermally accessible conformational states, which represent local minima of a complex free-energy landscape.

MATERIALS AND METHODS

NMR Structure Refinement. For conformational analysis, NMR experiments were carried out at 295 K on a Bruker DMX 750 spectrometer. Resonance assignments were performed according to the method of Wüthrich (*8*). The 2D-TOCSY spectra were recorded with spin-lock periods of 70 ms using the MLEV-17 sequence for isotropic mixing (*44*). Experimental interproton distance constraints were extracted from 2D-ROESY experiments (*45*) with mixing times of 200 ms. Dihedral angles constraints were extracted from 2D-DQF−COSY (*46*) and simple ^{1}H-1D spectra. All molecules were measured in deuterated dimethyl sulfoxide (DMSO).

Distance geometry (DG) and molecular dynamics-simulated annealing (MD-SA) calculations were performed with the INSIGHTII (version 98.0) software package from MSI on Silicon Graphics O2 R5000 computers. For each of the investigated azopeptides, 100 structures were generated from the distance-bound matrixes. Triangle-bound smoothing was used. The NOE intensities were converted into interproton distance constraints using the following classification: very strong (vs) 1.7−2.3 Å, strong (s) 2.2−2.8 Å, medium (m) 2.6−3.4 Å, weak (w) 3.0−4.0 Å, very weak (vw) 3.2−4.8 Å, and the distances of pseudoatoms were corrected as described by Wüthrich (*8*). The $^3J_{HN-H\alpha}$ coupling constants were converted into constraints for the backbone ϕ dihedral angles using the Karplus relation. Multiple discrete ranges were used for the ϕ torsion angle restraints when multiple nonoverlapping solutions exist for the Karplus equation taking into account experimental error and 10° uncertainty from the Karplus parameters. The structures were generated in four dimensions and then reduced to three dimensions with the EMBED algorithm and optimized with a simulated annealing step according to the standard protocol of the DG II package of INSIGHT II. All 100 structures were refined with a short MD-SA protocol. After an initial minimization, 5 ps at 300 K was simulated followed by exponential cooling to ∼0 K during 10 ps. A time step of 1 fs was used with the CVFF force field, while the solvent DMSO was accounted for by assuming a dielectric constant of 46.7. The experimental constraints were applied at every stage of the calculation with 50 kcal mol^{-1} Å^{-2} for distance constraints and 50.0 kcal mol^{-1} rad^{-2} for coupling constants. For the 10 structures of lowest energy, the violations of experimental NOE constraints were all below 0.2 Å.

Unconstrained MD Simulations. For each of the model peptides in its two isomeric states, the NMR structure of lowest energy was chosen as the starting structure. The peptides were solvated with 960 molecules of DMSO in a rhombic dodecahedron with a radius of 2.7 nm. All solvent molecules within 2 Å of any peptide atom were removed. Version 22 of the CHARMM all-atom force field (*47*) was employed for the peptide moiety. The force field was supplemented by parameters for the azobenzene dye and its linkage into the peptide backbone, which were derived from DFT calculations (*43*). A united-atom model was chosen for the DMSO molecules (*48*). Periodic boundary conditions were imposed. The long-range electrostatic interactions were treated by a moving boundary reaction field method (*49*) based on fast hierarchical multipole expansions (*50*). Up to a distance of 1.3 nm, the Coulomb sum was evaluated explicitly, while at larger distances, charge groups were represented by their dipoles and quadrupoles. At distances beyond 2.5 nm, a dielectric continuum with the experimental dielectric constant of DMSO, 45.8, was assumed and its influence was included by analytical reaction field forces (*49*). The Lennard−Jones interactions were evaluated explicitly up to a distance of 13 Å, and a long-range correction

to the Lennard−Jones energy was applied. The equations of motion were integrated by a multiple time-step algorithm (*51*) with a time step of 1 fs. The bond lengths of all hydrogens and the geometries of the DMSO molecules were kept constant using the MSHAKE algorithm (*52*). The selected temperature and a pressure of 1 atm were maintained by a Berendsen thermostat and barostat (*53*) with coupling constants of 1 and 5 ps.

During the first 100 ps of MD simulation at 298 K, the peptides were kept fixed so that the DMSO molecules could adapt to the solute. This adaptation was followed by a 50 ps simulation in which harmonic position restraints were imposed to the C_α atoms and by 100 ps of unconstrained simulation during which the systems were heated to 500 K. Starting from this state, trajectories of 50 ns duration each were calculated. The elevated simulation temperature was chosen to enable a statistically sufficient sampling of the configuration space during the time of simulation. During the total 300 ns of simulation time, the coordinates of the peptides were saved every 1 ps.

Note that the density in the 500 K simulation systems was 0.919 ± 0.002 g/cm^3, i.e., only 16.4% smaller than at 300 K. This value closely matches the 16.7% reduction expected from the thermal expansion coefficient of 8.2×10^{-4} K^{-1}, which has been determined for the employed DMSO model by 300 K simulations (*43*). These findings indicate that the liquid phase was maintained during our 500 K simulations. Correspondingly, the boiling point of our DMSO/peptide mixture is above 500 K, although the experimental boiling point of DMSO is at 462 K.

Determination of the Conformational Ensembles. For the analysis of the MD trajectories, the configurations of the octapeptides were described by the ϕ/ψ dihedral angles of the peptide backbone, resulting in time series of 16-dimensional feature vectors $\alpha \equiv (\phi_1, \psi_1, \phi_2, \psi_2, ..., \phi_8,$ and $\psi_8)$. On the basis of these time series and assuming ergodicity, we derived parametric and analytical models $\rho(\alpha)$ for the probability densities in the form of mixtures of 100 univariate Gaussian distributions with identical statistical weights and widths. The model parameters were optimized using a safely converging algorithm for the maximum-likelihood density estimation in high-dimensional data spaces (*54*, *55*) that was extended to circular variables, e.g., dihedral angles (*43*). From the estimated densities $\rho(\alpha)$, the free-energy surfaces (FESs) were derived as $\Delta G(\alpha) = -k_b T \ln(\rho(\alpha)/\rho_{max})$, were k_b denotes the Boltzmann constant, T denotes the temperature, and ρ_{max} denotes the estimated density maximum. The conformations k of the model peptides correspond to the local minima of the FES (*56*, *57*). To account for the hierarchy of subconformations and conformations, we constructed a scale space of successively smoothened FES by convolving the model density with a Gaussian of varying width σ. On each scaled FES, we employed a gradient descent to detect all local minima and hence the number $N(k;\sigma)$ and the prototypical geometries α_k of all conformations $k = 1, ..., N(k;\sigma)$ at the chosen resolution. Finally, each peptide geometry α encountered in the time series was classified by the same method as belonging to one of the conformations k found at a selected resolution.

Characterization of Conformations by Character Strings. Each conformational ensemble k is described by a string of seven α's and β's, derived from a classification of each of the seven non-Gly amino acid residues as being of either predominantly α-helical or β-strand geometry. A residue is classified as α helical, if the ψ dihedral angle at its C_α atom is in the range between $-130°$ and $25°$, and classified as β strand otherwise. A bold letter denotes a secondary structure motif that is conserved in more than 95% of all structures α associated to a given conformation k, whereas a gray letter indicates a local geometry that is found only in the simple majority of the associated structures. The residue Gly has been omitted from this classification because of the high flexibility of the peptide backbone at the corresponding C_α atom.

Principal Component Analysis (PCA) of Peptide Geometries in Angular Space. To identify those directions in the 16-dimensional angular configuration space, along which the cis and trans geometries of a given peptide may be discernible at best, we applied a PCA to data sets of peptide geometries α, which were obtained by combining the cis and trans trajectories. The well-known PCA method identifies those directions in high-dimensional data spaces, which are connected with the largest variances of the data. To formulate a PCA for circular variables α, we used

$$C_{i,j} = \langle \sin(\alpha_i - \bar{\alpha}_i)\sin(\alpha_j - \bar{\alpha}_j) \rangle$$

as one of the possible definitions (*43*, *58*) for the covariance matrix **C**. Here, $\langle ... \rangle$ stands for the average over the dataset, whereas $\bar{\alpha}_i$ denotes the ith component of the circular average (*58*) of the feature vector $\boldsymbol{\alpha}$. The principal components represent the desired directions and result from a diagonalization of **C** as the eigenvectors to the largest eigenvalues.

Observables for Comparison of MD Trajectories with NMR Raw Data. For comparison with NMR distance restraints derived from observed NOEs, we have calculated global and conformation-specific proton−proton interaction distances d_{ij} from the MD trajectories as follows. After assigning each structure sampled by MD to one of the prototypical conformations k extracted from the trajectories, we have calculated the conformation-specific interproton distance distributions $p_k(r_{ij})$ as histograms and the statistical weights P_k of the conformations by simple counting. The total distance distribution $p(r_{ij})$ is then obtained as a suitably weighted sum over $p_k(r_{ij})$. Because the NOE is a dipole−dipole interaction, we have calculated interaction distances d_{ij} from these distributions by the prescription

$$d_{ij} = \langle r^{-6}_{ij} \rangle^{-1/6}$$

where the brackets $\langle ... \rangle$ denote either conformation-specific or global expectation values referring to $p_k(r_{ij})$ or $p(r_{ij})$, respectively (see refs *25* and *59* for an explanation of this prescription).

RESULTS AND DISCUSSION

MD Time Series Indicate a Conformational Dynamics. As an example for the raw data that were collected during the MD simulations, Figure 2 shows the time series (gray) of two dihedral angles in the backbone of the model peptide *cis*-cAPB (see Figure 1). Parts of the time series are color-coded pointing to the three backbone conformations of lowest free energy, which were determined by gradient descent on

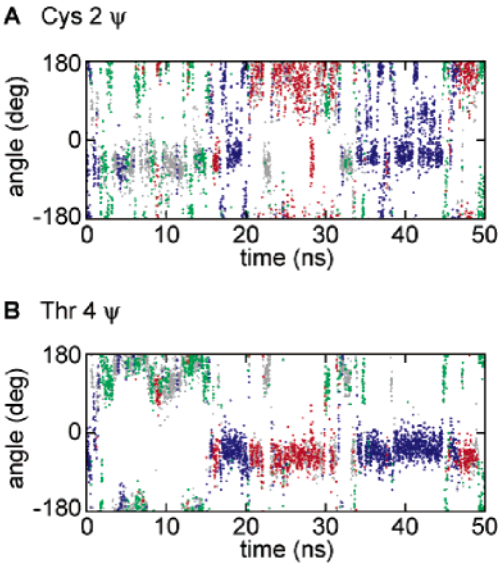

FIGURE 2: Time series (gray) for two backbone dihedral angles of *cis*-cAPB obtained by the MD simulation. Colors classify those parts of the MD trajectory, which belong to the three conformations of lowest free energy shown in Figure 7.

the scaled maximum likelihood estimate $\Delta G(\alpha)$ of the FES using the method introduced above and are depicted in Figure 7. In accordance with Figure 2, frequent jump-like transitions on the subnanosecond time scale take place at the angle ψ of residue Cys 2, whereas the corresponding angle of residue Thr 4 exhibits longer periods of relative stability. Concerning the three color-coded conformations of low free energy, according to Figure 2A, the angle ψ at Cys 2 does not contribute to their distinction. In contrast, Figure 2B shows that the angle ψ at Thr 4 separates the green conformation from the blue and red conformations. Altogether, Figure 2 demonstrates that the MD simulations sample a variety of meta-stable conformations of the model peptides.

Ramachandran Projections of the FES. A first insight into the structural ensembles of the three model peptides is given by Figure 3, which presents the free-energy landscapes (FESs) computed from the 500 K equilibrium MD trajectories. To enable two-dimensional representations of the 16-dimensional FES, Ramachandran plots, i.e., projections onto the eight pairs of backbone dihedral angles, are used. In each subfigure, the FES of the cis (red) and trans isomers (blue) are superimposed to enable a direct comparison and an assessment of the effect that the isomerization of the azobenzene dye has on the peptide backbone. Within the FES of *cis*-cAPB (Figure 3A, red), two energy minima exist for all residues except for the highly flexible Gly 7. In accordance with the classification scheme of conformations by seven-character strings introduced in the Materials and Methods, we denote an energy minimum with ψ in the range of approximately -130 to 25° as being α-helical and a minimum with values of ψ in the vicinity of 170° as of extended or β-strand geometry. Obviously, from the FES of *cis*-cAPB neither pure α-helical nor pure β-strand secondary-structure motifs can be deduced for the peptide backbone. In particular, conclusions on the structures of the underlying meta-stable conformations cannot be obtained, because the projected FES shown here lack all information concerning the correlation between the coordinates of different residues. Yet Figure 3 allows a first comparison between the energy

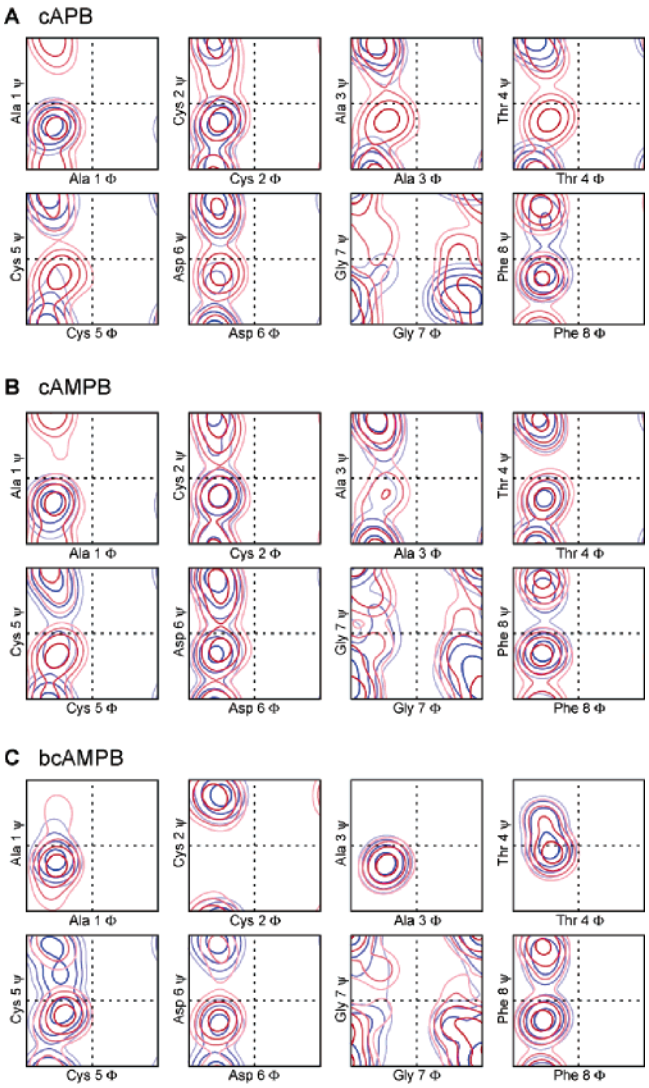

FIGURE 3: Ramachandran plots of the energy landscapes derived by maximum likelihood density estimates $\rho(\alpha)$ from the MD simulations. For all three model peptides and both for the cis (red) and trans (blue) isomers, the free energy is shown as a function of the backbone dihedral angles ϕ and ψ. Contours represent 1 kcal/mol.

landscapes of the isomeric states of cAPB. Here, for the trans isomer (Figure 3A, blue), a structural variability is observed only at the residues Cys 2, Asp 6 and Phe 8, whereas the residues 3−5 are locked in an extended β-strand configuration. Thus, Figure 3A demonstrates that in the model peptide cAPB a switching of the azobenzene dye strongly changes the free-energy landscape of the peptide backbone.

A comparison of parts A and B of Figure 3 allows an assessment of the effect of the inclusion of the methylene spacer into the cyclic peptides (see Figure 1). The FES of *cis*-cAMPB closely resembles that of *cis*-cAPB. On the other hand, the spacer loosens the restrictions imposed on the peptide moiety by the trans chromophore, as can be seen by the appearance of α-helical geometries at the residues 3−5 of *trans*-cAMPB (Figure 3B, blue).

Next, Figure 3C suggests that the closure of the disulfide bridge in bcAMPB (see Figure 1) leads in both isomers to a pronounced stiffening of the peptide backbone at the residues 2−4, whose geometry exhibits no variation at all except for thermal fluctuations. Therefore, in the case of bcAMPB, the

ability of the chromophore to influence the conformational space of the backbone moiety is quite limited.

In summary, Figure 3 demonstrates that the method employed for a statistical data analysis of MD trajectories is capable of generating a smooth, analytical, and generalized representation of the FES. Furthermore, first insights into conformational properties of the different model peptides could be deduced from the two-dimensional Ramachandran projections of the FES.

But, as pointed out above, the projections of the FES used in Figure 3 neglect all correlations between the dihedral angles of different residues. A method to identify such correlations is the PCA. The PCA has frequently been employed before to analyze MD trajectories (*60*−*64*). However, to our knowledge, an application of the PCA to circular data spaces spanned by angular variables has not yet been presented before. In the Materials and Methods, the PCA is formulated for this case. When applied to each of the model peptides, a PCA of the dataset {α}, which combines the cis and trans trajectories, should detect those directions in the 16-dimensional space of dihedral angles, which best separate the conformational spaces of the two isomers.

Principal Component Projections of the FES. Figure 4 shows the projections of the estimated FES (cis in red and trans in blue) on the first two principal components for each member of the family of model peptides. Both contour plots (left) and pseudo-3D surfaces (right) are presented. Furthermore, the locations of the conformations, which were identified by gradient descent as described further below and are numbered according to increasing free energy, are indicated by filled circles.

In Figure 4A an extended energy landscape is observed for *cis*-cAPB, in which the local minimum corresponding to the conformation of lowest free energy *G* is separated by a barrier of approximately 1 kcal/mol from a broad basin comprising the other conformations. In contrast, the projected FES of *trans*-cAPB is more compact and contains only a single global minimum corresponding to only one conformation. Together with the observation that the centers of the two FES or, equivalently, probability distributions are actually separated by the collective coordinates given by the first two principal components, Figure 4A again shows that the isomeric state of the chromophore shapes the conformational landscape of the model peptide cAPB.

On the basis of this result, Figure 4B confirms the earlier observation that the inclusion of the methylene spacer into the peptide cAMPB leads to a relaxation of the restrictions imposed on the trans isomer by the chromophore; the principal component projection of the corresponding FES (blue) is more extended than in the case of *trans*-cAPB, and a second local minimum indicating an alternative conformation appears. Moreover, a stronger overlap between the cis and trans FES is observed for cAMPB than for cAPB.

As is apparent also in the principal component projection, the closing of the disulfide bridge in bcAMPB (Figure 4C) has the strongest impact on the FES of the peptide, which becomes highly rugged for both isomers exhibiting high barriers between the different conformations. Because the two projected cis and trans FES fully overlap and are equally extended, one can conclude that for bcAMPB the cis−trans

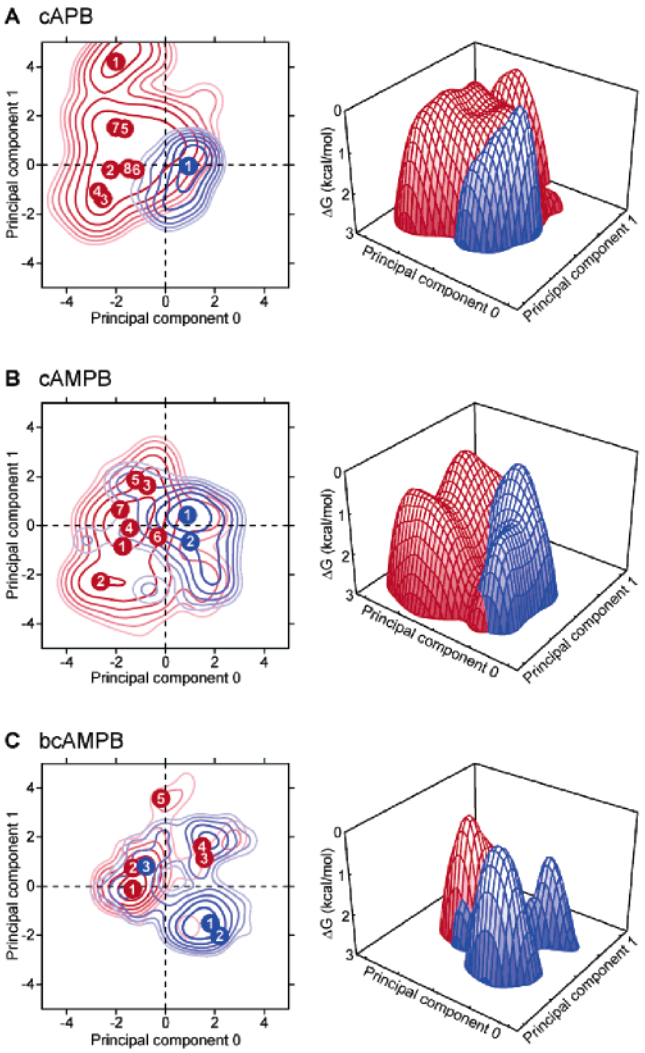

FIGURE 4: Projection of the high-dimensional energy landscapes onto their first two principal components. Both contours, representing 0.5 kcal/mol each, and pseudo-3D plots are shown for the cis (red) and trans (blue) isomers. Filled circles with numbers indicate the geometries of the conformations presented in Figure 6.

isomerization of the chromophore can only marginally alter the FES of the peptide backbone.

Identification of Conformations by Hierarchical Cluster Analysis. Even though the two-dimensional projections of the FES shown in Figures 3 and 4 give some insights into the range and topology of the conformational landscapes of the various peptides, a thorough exploration of the FES and hierarchy of conformations cannot be derived from these low-dimensional projections. Therefore, Figure 5 presents, as a function of a spatial scale σ, the respective number of conformations that were detected in the correspondingly smoothened 16-dimensional FES by the gradient descent approach introduced in the Materials and Methods.

At large values of the smoothening scale σ, each of the FES exhibits only a single minimum, which marks the average backbone structure. Therefore, all curves in Figure 5, when followed from right (strong smoothening and low resolution) to left (diminished smoothening and high resolution of the FES), start at the value one. Correspondingly, the decrease of the scale σ and the correspondingly better resolved representations of the FES lead to the identification of successively more local minima, i.e., conformations. Here,

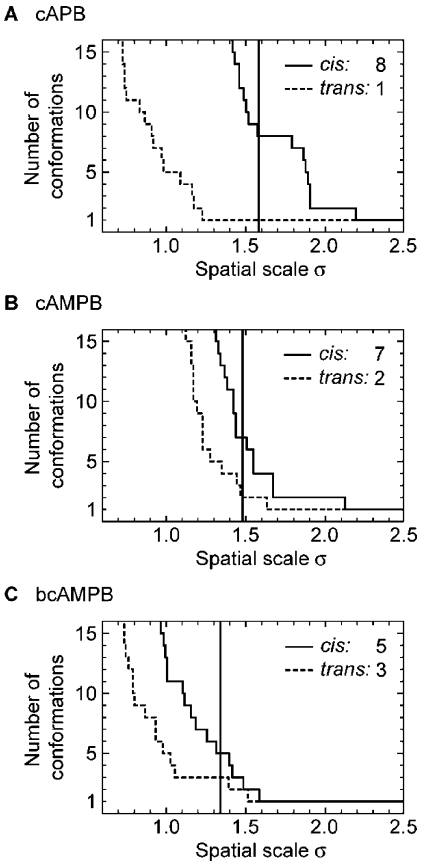

FIGURE 5: Numbers of conformations identified by gradient descent on the smoothened 16-dimensional FES as a function of the spatial scale σ used for smoothening. The vertical line indicates for each member of the family of model peptides the scale that was chosen for the detailed analysis of the conformational ensemble. The numbers of conformations identified at this selected scale are given in the insets.

broad σ intervals, in which a constant number of conformations is detected, indicate well-defined and stable sets of conformational substates. In Figure 5A, examples are the partitioning of the FES of *cis*-cAPB (—) into two or eight conformations and the prevalence of a single conformation for *trans*-cAPB over a wide range of the scale σ (- - -). Furthermore, the relative shapes and positions of the two curves enable another estimate for the influence of the chromophore isomerization on the conformational landscape of the peptides: while in the case of cAPB, the splits of the cis and trans isomers into many separate conformations take place at strongly different values of the scale σ, the cis and trans curves for cAMPB (Figure 5B) are less differentiated. Additionally, the shift of the conformational splitting to smaller values of σ observed in Figure 5C indicates once again the compactness of the FES of the two isomers of bcAMPB.

Because a discussion of all molecular structures associated with all conformations detected at all spatial scales is not feasible, we have chosen a single scale for each of the three peptide species for further discussion. This somewhat arbitrary choice is indicated in Figure 5 and was guided by the aim to select similar scales, stable sets of conformations, and a low total number of molecular structures.

Comparison of MD Conformations and NMR Structures. Figure 6 presents these prototypical MD conformations and enables a comparison with the NMR structures. The NMR structures of cAPB and cAMPB shown here have been reported before (*38*, *39*), while the refined structures for bcAMPB represent a new result derived from the NMR measurements described above. In fact, an initial disagreement between our MD results and published NMR structures inspired us to a refinement using NMR data recorded at higher magnetic field strength. The thus obtained NMR data of higher quality agree much better with the MD ensembles.

In Figure 6A, the MD conformations are drawn using a tube representation for the peptide backbone and the azobenzene dye. The employed gray scale is given in the lower left corner of the figure and indicates the relative free energies of the conformations as calculated from their relative populations within the MD trajectories. To align the molecular structures, a root-mean-square deviation fit on the average structure was performed.

Starting with the model peptide *trans*-cAPB, Figure 6 reveals a certain agreement between the MD and NMR structures. In accordance with both results, the azobenzene dye enforces an elongated geometry of the peptide backbone that has no conformational freedom left. Only for the orientation of the phenyl rings of the chromophore is a striking difference between the experimental and simulated structures quite obvious. However, experimental NMR data contain no information on the orientation of the phenyl rings of the azobenzene moiety. On the NMR time scale (slower than milliseconds), the rings may rotate so that protons from opposite sides are magnetically equivalent. In the NMR structure calculations, they are represented by pseudoatoms, which are located on the rotation axis of the rings such that the corresponding constraints do not directly influence the final ring orientation. Because the force field and the molecular model employed in these NMR structure calculations are much less sophisticated than those of the unconstrained MD simulations, different orientations are not surprising. For instance, the MD simulations include a microscopic model for the solvent, whereas the NMR refinement force field applies a continuum description.

For the cis isomer of cAPB, the MD simulations predict a helical conformation (black) as the state of lowest free energy, which also appears in the NMR structures. The other seven MD conformations identified by gradient descent on the 16-dimensional FES display varying geometries, which include looplike backbone arrangements in various parts of the peptide. This high variability of *cis*-cAPB is not evident in the NMR structures, whose ensemble appears to be more compact.

As discussed before, the inclusion of the methylene spacer into cAMPB loosens the restrictions on the peptide backbone exerted by the trans chromophore. In accordance with the NMR structures (Figure 6B, *trans*-cAMPB), this loosening leads to a helical arrangement of the peptide and a bent geometry of the azobenzene dye. In contrast, the corresponding MD results still predict an extended β strand for the peptide in the main conformation (black). Here, in comparison to *trans*-cAPB, the appearance of a second conformation, in which the peptide backbone exhibits an additional turn, points toward the increased flexibility. In accordance with the MD results and in contrast to the NMR structures, the trans chromophore is planar in both conformations.

The NMR structures of *cis*-cAMPB are mostly helical and again very compact, whereas MD predicts conformations of

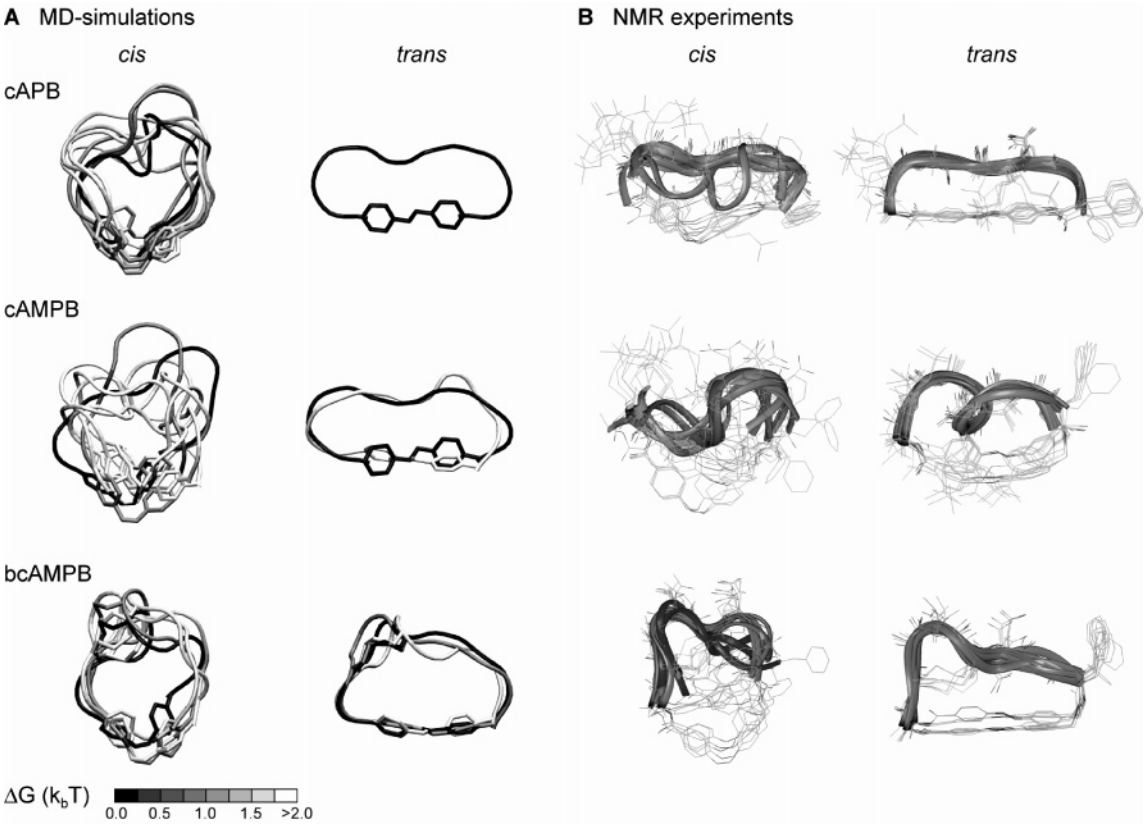

FIGURE 6: (A) Peptide conformations derived from the MD simulations. The peptide backbone is represented by a tube connecting the C_α atoms, while the gray level indicates the relative free energy of the respective conformation (see the scale in the lower left corner). The plots were generated using VMD (*66*). (B) Structures from the NMR refinement as published before for cAPB (*38*) and cAMPB (*39*). The structures for bcAMPB are new results presented here.

a very large variability, which is even larger than in *cis*-cAPB. Thus, for both isomers of the very flexible cAMPB peptide, notable differences exist between the freely simulated and experimentally derived structures. For this peptide, the NMR analysis was hampered by the existence of multiple minor conformations overlapping with the dominant major conformation. While the NMR NOE data of cAMPB still agree with the MD ensembles (see below), it appears that for this peptide conventional NMR structure calculations do not lead to realistic conformational ensembles in both isomeric forms.

For the bcAMPB peptide, however, whose conformational space is strongly restricted by the disulfide bridge, the MD conformations and the newly presented NMR structures agree quite well. Both methods give similar molecular geometries and predict conformational ensembles, in which the cis isomer exhibits a flexibility that is only marginally larger than that for the trans isomer.

Summarizing the comparisons depicted in Figure 6, we may state that the differences between the simulated and experimentally derived structures of the peptide backbone increase with increasing flexibility of the peptide. They are quite small for the bcAMPB peptide, which is strongly restrained by the disulfide bridge in both isomeric states, and for the *trans*-APB peptide, in which the elongated chromophore and its stiff linkage to the peptide enforces an extended β-strand conformation. They become larger for *trans*-cAMPB because of its flexible methylene spacer between the chromophore and the peptide and become notably large for *cis*-cAPB and *cis*-cAMPB, in which the cyclization with the bent cis chromophore poses hardly any constraints to the peptide conformations. Here, in particular, the backbone structures predicted by NMR refinement are much more compact than the conformations sampled by MD. Furthermore, the geometry and orientation of the chromophore is described differently by the two approaches, particularly in the case of the *trans*-cAPB and *trans*-cAMPB peptides.

Concerning the structure of the peptide backbone, an even more detailed insight into the differences between the MD and NMR results can be obtained, if one analyzes the various MD conformations individually one by one. For this purpose, we concentrate on the example of the quite flexible *cis*-cAPB, in which these differences were seen to be particularly pronounced.

MD Conformations of c-APB. Figure 7 provides an overview over the individual conformations of cAPB, which have been extracted as prototypical structures from the MD trajectory. Also shown are sets of structural snapshots randomly selected from the MD trajectory, which belong to the respective conformations. The sizes of these snapshot sets are chosen according to the statistical weights of the conformations in the ensemble and are kept low enough as to enable a visual distinction. In addition, each conformation is characterized by a seven-character string coding the local geometry of the peptide at the C_α atoms of the non-Gly residues, where α stands for a local α helical and β stands for a local β-strand-type geometry (see the Materials and Methods for details particularly concerning the meaning of bold characters).

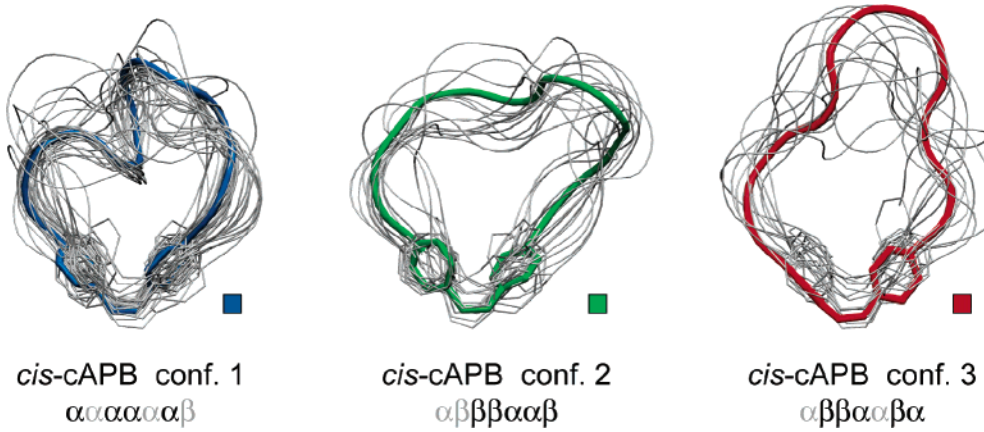

FIGURE 7: Three main conformations of cAPB (thick tubes) and associated structures from the MD simulations (thin tubes). As explained in the Materials and Methods, each conformation is described by a string of α's and *β*'s, derived from a classification of each of the seven amino acid residues (excluding the Gly) as being either of α-helical or *β*-strand geometry.

The first conformation (blue) of *cis*-cAPB is essentially helical, as can be seen by inspecting Figure 7 and is confirmed by the characterizing string ααααααβ. Thus, the native α-helical structure of the octapeptide within the protein thioredoxin reductase is essentially preserved within the cyclic APB peptide as long as the azobenzene chromophore is in its bent cis-isomeric state. A close inspection of the various molecular snapshots (gray) associated with conformation 1 reveals two subconformations that differ in the vicinity of the residues 5−8. At a finer scale of our conformational analysis, the blue conformation will thus split into these two subconformations.

Considering the prototypical structures of the next and slightly less populated conformations 2 and 3 identified in the MD trajectory of *cis*-cAPB, which in Figure 7 are marked by green and red colors, respectively, we immediately see that they are more extended than conformation 1. Conformation 2 is characterized by the string α*βββ*αα*β* and exhibits a turn-like geometry at the residues 5 and 6, directed into the direction of the observer. A similar feature can be observed in conformation 3, whose characterizing string α*ββ*αα*β*α assigns the turn to the residues 4 and 5 and thus locates that turn at a larger distance from the azobenzene moiety. The remaining MD conformations 4−8 are less and less populated and have varying looplike structures. For instance, the characteristic string α*ββ*αα*ββ* of conformation 4 shows that this conformation differs from the red conformation 3 essentially by a α → *β* transition at Phe-8.

A comparison of the cAPB conformations predicted by MD and depicted in Figure 7 with the corresponding NMR structures shown in Figure 6 now reveals that solely the compact MD conformations, i.e., the blue conformation 1 of *cis*-cAPB and the single conformation of *trans*-cAPB, resemble the corresponding NMR structures. In contrast, the remaining extended looplike MD conformations of *cis*-cAPB find no correspondence among the NMR structures. This conformation-local statement on the similarity between compact MD conformations and NMR structures sharpens our previous observation stated in connection with Figure 6, where we had seen that the mechanically constrained and correspondingly compact MD conformations of the bicyclic peptide bcAMPB agree quite well with the associated NMR structures.

Reasons for Structural Differences. Now the question on the causes of the thus characterized structural differences must be addressed. Here, one could first speculate that the occurrence of extended looplike structures in MD and their absence in NMR is due to the different thermodynamic conditions at which the respective ensembles have been obtained. The MD conformations were sampled at a temperature of 500 K, whereas the NMR data were obtained at 295 K and at a 17% larger density (see the Materials and Methods), suggesting that in MD the folding of the peptide into compact conformations may be prevented by the high temperature. Admittedly, the elevated temperature and reduced density applied in our MD simulation to achieve a more rapid sampling of the conformational space will contribute to the stated structural differences. However, these altered thermodynamic conditions cannot explain the structural differences completely or to the largest part. For an explanation consider, e.g., the free energies of the extended and looplike conformations 2 and 3 of *cis*-cAPB, which are less than k_bT (1 kcal/mol) larger than that of the energetically most favorable and α-helical conformation 1 (cf. also Figure 6). If these free-energy differences were exclusively due to different entropies of the conformations, then a temperature reduction from 500 to 300 K would leave their relative populations invariant. This scenario is plausible, because the characterizing strings of the three conformations displayed in Figure 7 suggest that conformations 2 and 3 are more rigid than conformation 1, because they have one thermally flexible ψ angle (normal face symbol) less. On the other hand, if the free-energy differences were due to different enthalpies of the conformations, then the 17% density increase upon temperature reduction would lead to corresponding enthalpy increases, because the contributing binding interactions are distance- and, therefore, density-dependent. Correspondingly, one can expect the free-energy differences to increase by about the same percentage. However, because according to MD the free-energy differences are smaller than 1 kcal/mol at 500 K, the conformations 2 and 3 will be populated also at 295 K.

Next, one might suspect that errors in the peptide force field, in the solvent model, or in the treatment of the electrostatics used in the MD simulation favor unphysical conformations, here. To answer this question, one should

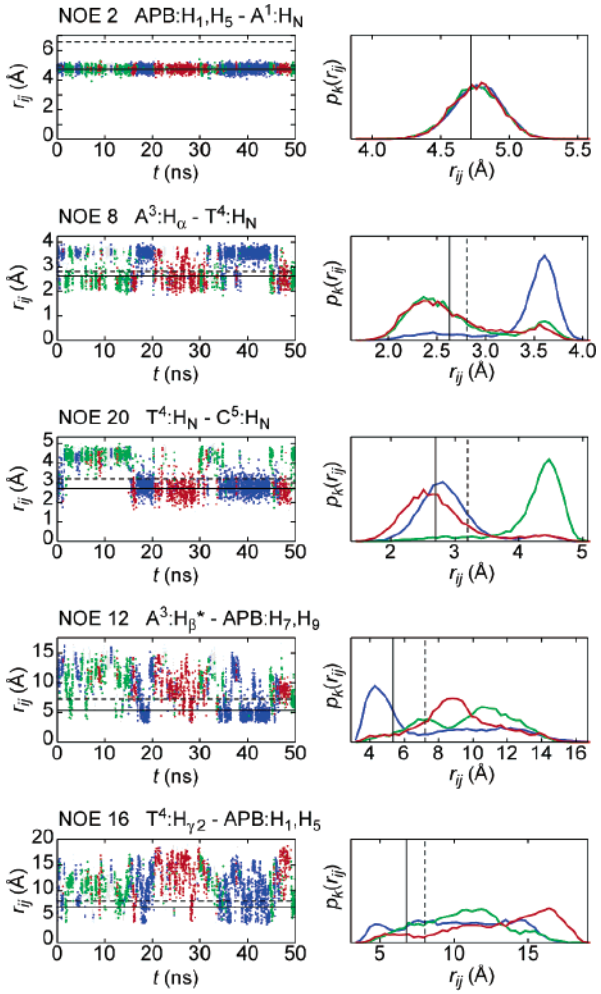

FIGURE 8: Five atom distances r_{ij}, as observed in the unconstrained MD simulation of *cis*-cAPB, are compared to the corresponding NMR-derived interproton distance restraints (*38*) (NOEs characterized by "*NOE number residue 1:proton−residue 2:proton*"; for the numbering of the APB protons, see Figure 1). Time series of the distances r_{ij} (left) and plots of the conformation-specific distance distributions $p_k(r_{ij})$ (right) are shown. Colors code the three conformations k highlighted in Figure 7. (- - -) NMR upper limits $d_{ij,\max}$. (—) Trajectory averages $d_{ij} = \langle r^{-6}{}_{ij}\rangle^{-1/6}$.

check whether the calculated *ensemble* of MD conformations is compatible with the *raw* NMR data (e.g., the interproton distance restraints derived from the observed NOE intensities), from which the NMR structures were calculated by simulated annealing.

Comparison of MD Trajectory with NMR Data. To carry out such a check, we have evaluated the interproton distances r_{ij} for each structure sampled by the MD trajectories, assigned each of these structures to one of the prototypical conformations k extracted from the trajectories, and calculated the conformation-specific distance distributions $p_k(r_{ij})$ as well as the total distance distributions $p(r_{ij})$ from these data. Using these distributions, we have finally calculated effective proton−proton interactions distances $d_{ij} = \langle r^{-6}{}_{ij}\rangle^{-1/6}$ as described in the Materials and Methods. The Supporting Information compares for each isomeric state of the three model peptides the NMR restraints with the conformation-specific and total MD interaction distances.

As an example, Figure 8 shows for *cis*-cAPB the time series of five selected interproton distances and the distributions $p_k(r_{ij})$ of these distances for the three conformations k highlighted by color coding as in Figure 7. For comparison, the corresponding upper distance limits $d_{ij,\max}$ derived from the NOE intensity (- - -) and the MD interaction distances d_{ij} obtained from the total distance distribution $p(r_{ij})$ (—) are shown in each graph. Although in principle the absence of an NMR NOE signal could also contain useful information, it has turned out from many structural NMR studies that lower bounds are very difficult to establish with accuracy. For purely technical reasons related to the acquisition of the NMR spectra as well as because of intrinsic properties of the given peptide (local dynamics and conformational fluctuations), NOE signals can be considerably attenuated or even completely absent despite spatial closeness of hydrogen nuclei. Therefore, lower bounds were not considered in our case.

A first glance at the locations of the horizontal lines in the graphs at the left of Figure 8 (and at the vertical lines at the right) immediately reveals that in all cases the MD interaction distances d_{ij} are smaller than the corresponding upper NMR distance limits $d_{ij,\max}$. Therefore, the total MD ensemble is very well compatible with the raw NMR data in all shown cases despite the fact that the refined NMR structures of *cis*-cAPB are much more compact than the conformations and peptide structures sampled by MD (cf. Figures 6 and 7).

This remarkable result raises the questions of how such an excellent agreement can arise and what it tells us about the occurrence or nonoccurrence of the open-loop structures predicted by MD and apparently suppressed by the simulated annealing technique applied in NMR refinement. These questions find different answers for each of the five observables depicted in Figure 8, which makes a detailed discussion necessary.

Consider first the topmost graphs referring to the NOE distance restraint number 2, which measures the distance between one of two equivalent protons (H1/H5) at one of the phenyl rings in the azobenzene dye (cf. Figure 1) and the amide proton H_N of the attached alanine residue. Because the covalent linkage between Ala-1 and the APB chromophore involves only one torsional degree of freedom, this distance is fixed by the covalent structure and the distance restraint must be trivially fulfilled for all conformations and any reasonable MM force field. Correspondingly, the three conformation-specific distance distributions $p_k(r_{ij})$ closely overlap, and the matching of the NMR distance restraint solely confirms that the MM modeling of the covalent linkage is reasonable. No additional structural information is gained in this case.

Consider next the distance distributions $p_k(r_{ij})$ associated with NOEs number 8 and 10. In both cases, the total distribution $p(r_{ij})$ is bimodal exhibiting one peak at small distances, which is associated with two of the three low-energy conformations and one at large distances, which belongs to the remaining conformation. Both NOEs refer to neighboring residues, and the corresponding interproton distance strongly depends on the local geometry of the first of the two consecutive residues.

NOE 8 pertains to the residue pair Ala-3-Thr-4 and is of type $d_{\alpha N}$. Here, $d_{\alpha N} < 3$ Å indicates an extended geometry and larger values for a helical geometry at Ala-3 (*8*). In accordance with the classifying strings displayed in Figure 7, the green and red conformations are extended, whereas

the blue conformation is α helical at Ala-3. Correspondingly, the closely overlapping green and red distance distributions peak near 2.4 Å, and the dominant blue distribution $p_1(r_{ij})$ is centered at about 3.6 Å. Nevertheless, the distance restraint $d < d_{max} \approx 2.81$ Å is fulfilled by the ensemble, because the strong short-distance bias of the NOE interaction distance averaging ($d = \langle r^{-6}_{ij} \rangle^{-1/6}$) implies that a sizable admixture of conformations with a β-strand geometry at Ala-3 suffices for this purpose. In the NMR refinement, however, the inclusion of this distance restraint into the NMR refinement will exclusively and, therefore, erroneously enforce a β-strand geometry at Ala-3.

The NOE 20 refers to the residue pair Thr-4-Cys-5 and is of type d_{NN}, which has simply the reverse distance dependence; i.e., values $d_{NN} < 3$ Å indicate an α-helical geometry (like in the blue and red conformations) and larger values of an extended geometry (like in the green conformation) at Thr-4. Interestingly, also a quite strong NOE of type $d_{\alpha N}$ is observed for this residue pair (NOE 14, see the Supporting Information), which (i) means that in this case the NMR refinement is fed with conflicting structural information and (ii) confirms the conformational variability described by MD.

As opposed to the NMR data discussed so far, the NOEs 12 and 16 (cf. the lower part of Figure 5) report on true through-space distances between peptide residues and equivalent phenyl protons at the APB chromophore and, thus, carry information about the compactness of *cis*-cAPB. Here, the MD simulations predict very broad distance distributions $p_k(r_{ij})$, and nevertheless, the distance restraints are fulfilled by the ensemble. Only the helical conformation 1 has a short-distance peak for NOE 12. For both NOEs, the rare occurrence of short distances during the dynamics suffices for generating an NMR signal, because of the short-range bias of the NMR distance sampling. If the corresponding distance restraints are fed into the refinement, it will preferentially (and erroneously) generate compact structures. Furthermore, it will always try to impose all restraints to each individual structure and will neglect the fact that solely the whole conformational ensemble has to fulfill all restraints.

As documented in the Supporting Information, the MD ensemble of *cis*-cAPB fulfills 39 of the 41 observed NOE distance restraints. The two violated restraints belong to the proton pairs Thr-4:$H_{\gamma 1}$-Asp-6:$H_{\beta 1/2}$ and involve the only exchangeable OH proton $H_{\gamma 1}$ at Thr-4, which is found in the peptide. Because of small concentrations of water remaining in our DMSO solutions, proton exchange from the Thr-4-OH group to a nearby water molecule solvating Asp-6 cannot be excluded, which would lead to artificially enhanced intensities of the corresponding NOEs. Thus, the MD ensemble of *cis*-cAPB conformations is very well compatible with the NMR data despite the different temperatures used in the respective samplings. Please note that many more proton pairs than 41 give rise to NOE signals in the NMR spectra but only for 41 of those does the NOE signal not overlap with any other resonance of the spectrum, allowing for proper conversion into a spatial distance.

As a result of this quite detailed analysis, we are now able to answer the questions voiced above as follows: If a mixture of compact and open-loop structures, as predicted by MD for flexible peptides, is present in an NMR sample, the open structures become invisible because of the short-distance bias of the NOE. Thus, the main reason for the significant differences between the MD conformations and the NMR structures apparent in Figure 6 is the silent and, in the case of flexible peptide loops, erroneous assumption underlying the common NMR refinement procedures that the investigated peptide has only a single conformation (*9*−*18*). As soon as this assumption is violated, NMR will predict artificially compact and partially unphysical structures (*31*, *32*).

We would like to add that a similarly detailed analysis (*43*) of all of the MD and NMR data presented in the Supporting Information confirms this conclusion while giving additional insights into the effects of the temperature difference as well as into defects of the force fields employed in NMR refinement and MD sampling, respectively. However, these issues are well beyond the scope of this paper.

CONCLUSION

We have shown that small cyclic and bicyclic peptides can exhibit highly complex conformational dynamics, if the mechanical constraints imposed by the ring closures are not too severe. Then, they can serve as valuable models for biologically active surface loops where variable degrees of flexibility seem to serve for fine tuning and adjusting affinity and selectivity toward the ligand or receptor.

For a set of mechanically less constrained peptides, comprising mainly the cases of *cis*-cAPB and *cis*-cAMP, we have demonstrated that unconstrained MD simulations can not only reproduce the raw NMR data but also can yield a more detailed and more accurate insight into the conformational preferences than conventional NMR structure calculations, which cannot reproduce multiple open-loop structures occurring together with compactly folded structures.

A sophisticated cluster analysis proved essential for the mapping of the conformational free-energy landscape. While still being limited to small systems of a few amino acids and requiring special measures for a statistically significant sampling of the conformational space, unconstrained MD simulations can give for the experimentally difficult but biologically relevant cases of flexible peptide loops better and more realistic views of the structural properties than the usual NMR-based structure calculations.

Clearly, our brute force approach of using a strongly elevated temperature to enforce a statistically meaningful sampling of the conformational space is suboptimal and should be replaced by physically more appropriate sampling methods such as replica exchange (e.g., see ref *65*). Nevertheless, despite the corresponding temperature mismatch, the conformational ensemble sampled by MD turned out to be compatible with the NMR data. Experimental data are still required to check and improve theoretical descriptions. They allow the monitoring of slow processes that occur on time scales, which currently are beyond the reach of simulations because of computational limitations.

SUPPORTING INFORMATION AVAILABLE

Six tables listing NOE distance restraints measured for *cis*/*trans*-cAPB, -cAMPB, and -bcAPMB and global as well as conformation-specific interaction distances derived by MD. This material is available free of charge via the Internet at http://pubs.acs.org.

REFERENCES

1. Ulloa-Aguirre, A., Stanislaus, D., Janovick, J. A., and Conn, P. M. (1999) Structure−activity relationships of G protein-coupled receptors, *Arch. Med. Res. 30*, 420−435.
2. Pfaff, M. (1997) in *Integrin−Ligand Interaction* (Eble, J. A., and Kühn, K., Eds.) pp 101−113, Springer-Verlag, Heidelberg, Germany.
3. Yu, H., Rosen, M. K., Shin, T. B., Seidel-Dugan, C., Brugge, J. S., and Schreiber, S. L. (1992) Solution structure of the SH3 domain of Src and identification of its ligand binding site, *Science 258*, 1665−1668.
4. Tang, K. E. S., and Dill, K. A. (1999) How experiments see fluctuations of native proteins: Perspective from an exact model, *Int. J. Quantum Chem. 75*, 147−164.
5. Feher, V. A., and Cavanagh, J. (1999) Millisecond-time-scale motions contribute to the function of the bacterial response regulator protein Spo0F, *Nature 400*, 289−293.
6. Colson, A. O., Perlman, J. H., Smolyar, A., Gershengorn, M. C., and Osman, R. (1998) Static and dynamic roles of extracellular loops in G-protein-coupled receptors: A mechanism for sequential binding of thyrotropin-releasing hormone to its receptor, *Biophys. J. 74*, 1087−1100.
7. Hynes, R. O. (2002) Integrins: Bidirectional, allosteric signaling machines, *Cell 110*, 673−687.
8. Wüthrich, K. (1986) *NMR of Proteins and Nucleic Acids*, John Wiley and Sons, New York.
9. Olejniczak, E. T., Dobson, C. M., Karplus, M., and Levy, R. M. (1984) Motional averaging of proton nuclear Overhauser effects in proteins—Predictions from a molecular dynamics simulation of lysozyme, *J. Am. Chem. Soc. 106*, 1923−1930.
10. Kessler, H., Griesinger, C., Lautz, J., Muller, A., van Gunsteren, W. F., and Berendsen, H. J. C. (1988) Conformational dynamics detected by nuclear magnetic resonance NOE values and J-coupling constants, *J. Am. Chem. Soc. 110*, 3393−3396.
11. Abseher, R., Lüdemann, S., Schreiber, H., and Steinhauser, O. (1994) Influence of molecular motion on the accuracy of NMR-derived distances—A molecular dynamics study of 2 solvated model peptides, *J. Am. Chem. Soc. 116*, 4006−4018.
12. Brüschweiler, R., and Case, D. A. (1994) Characterization of biomolecular structure and dynamics by NMR cross-relaxation, *Prog. NMR Spectrosc. 26*, 27−58.
13. Constantine, K. L., Mueller, L., Andersen, N. H., Tong, H., Wandler, C. F., Friedrichs, M. S., and Bruccoleri, R. E. (1995) Structural and dynamic properties of a β-hairpin-forming linear peptide. 1. Modeling using ensemble-averaged constraints, *J. Am. Chem. Soc. 117*, 10841−10854.
14. Cuniasse, P., Raynal, I., Yiotakis, A., and Dive, V. (1997) Accounting for conformational variability in NMR structure of cyclopeptides: Ensemble averaging of interproton distance and coupling constant restraints, *J. Am. Chem. Soc. 119*, 5239−5248.
15. Melacini, G., Zhu, Q., and Goodman, M. (1997) Multiconformational NMR analysis of sandostatin (octreotide): Equilibrium between β-sheet and partially helical structures, *Biochemistry 36*, 1233−1241.
16. Baysal, C., and Meirovitch, H. (1998) Determination of the stable microstates of a peptide from NOE distance constraints and optimization of atomic solvation parameters, *J. Am. Chem. Soc. 120*, 800−812.
17. Schneider, T. R., Brunger, A. T., and Nilges, M. (1999) Influence of internal dynamics on accuracy of protein NMR structures: Derivation of realistic model distance data from a long molecular dynamics trajectory, *J. Mol. Biol. 285*, 727−740.
18. Bürgi, R., Daura, X., Mark, A., Bellanda, M., Mammi, S., Peggion, E., and van Gunsteren, W. (2001) Folding study of an Aib-rich peptide in DMSO by molecular dynamics simulations, *J. Pept. Res. 57*, 107−118.
19. Ponder, J. W., and Case, D. A. (2003) Force fields for protein simulation, *Adv. Protein Chem. 66*, 27−85.
20. Tavan, P., Carstens, H., and Mathias, G. (2005) in *Protein Folding Handbook* (Buchner, J., and Kiefhaber, T., Eds.) Vol. 1, pp 1166−1191, Wiley-VCH, Weinheim, Germany.
21. van Gunsteren, W. F., and Berendsen, H. J. C. (1990) computer simulation of molecular dynamics—Methodology, applications, and perspectives in chemistry, *Angew. Chem., Int. Ed. 29*, 992−1023.
22. Brooks, C. L. (2002) Protein and peptide folding explored with molecular simulations, *Acc. Chem. Res. 35*, 447−454.
23. Karplus, M., and McCammon, J. A. (2002) Molecular dynamics simulations of biomolecules, *Nat. Struct. Biol. 9*, 646−652.
24. Daura, X., van Gunsteren, W. F., and Mark, A. E. (1999) Folding-unfolding thermodynamics of a β-heptapeptide from equilibrium simulations, *Proteins 34*, 269−280.
25. Daura, X., Gademann, K., Schafer, H., Jaun, B., Seebach, D., and van Gunsteren, W. F. (2001) The β-peptide hairpin in solution: Conformational study of a β-hexapeptide in methanol by NMR spectroscopy and MD simulation, *J. Am. Chem. Soc. 123*, 2393−2404.
26. Stocker, U., and van Gunsteren, W. F. (2000) Molecular dynamics simulation of hen egg white lysozyme: A test of the GROMOS96 force field against nuclear magnetic resonance data, *Proteins 40*, 145−153.
27. Arthanari, H., McConnell, K. J., Beger, R., Young, M. A., Beveridge, D. L., and Bolton, P. H. (2003) Assessment of the molecular dynamics structure of DNA in solution based on calculated and observed NMR NOESY volumes and dihedral angles from scalar coupling constants, *Biopolymers 68*, 3−15.
28. Li, A. J., and Daggett, V. (1995) Investigation of the solution structure of chymotrypsin inhibitor 2 using molecular dynamics: Comparison to X-ray crystallographic and NMR data, *Protein Eng. 8*, 1117−1128.
29. Lei, H. X., and Smith, P. E. (2003) The effects of internal water molecules on the structure and dynamics of chymotrypsin inhibitor 2, *J. Phys. Chem. B 107*, 1395−1402.
30. Colombo, G., Roccatano, D., and Mark, A. E. (2002) Folding and stability of the three-stranded β-sheet peptide betanova: Insights from molecular dynamics simulations, *Proteins 46*, 380−392.
31. Stote, R. H., Dejaegere, A. P., Lefevre, J. F., and Karplus, M. (2000) Multiple conformations of RGDW and DRGDW: A theoretical study and comparison with NMR results, *J. Phys. Chem. B 104*, 1624−1636.
32. Lee, M. R., and Kollman, P. A. (2001) Free-energy calculations highlight differences in accuracy between X-ray and NMR structures and add value to protein structure prediction, *Structure 9*, 905−916.
33. Philippopoulos, M., and Lim, C. (1999) Exploring the dynamic information content of a protein NMR structure: Comparison of a molecular dynamics simulation with the NMR and X-ray structures of *Escherichia coli* ribonuclease HI, *Proteins 36*, 87−110.
34. Prompers, J. J., and Brüschweiler, R. (2001) Reorientational eigenmode dynamics: A combined MD/NMR relaxation analysis method for flexible parts in globular proteins, *J. Am. Chem. Soc. 123*, 7305−7313.
35. Dvorsky, R., Hornak, V., Sevcik, J., Tyrrell, G. P., Caves, L. S. D., and Verma, C. S. (2002) Dynamics of Rnase Sa: A simulation perspective complementary to NMR/X-ray, *J. Phys. Chem. B 106*, 6038−6048.
36. Prabhu, N. V., Lee, A. L., Wand, A. J., and Sharp, K. A. (2003) Dynamics and entropy of a calmodulin−peptide complex studied by NMR and molecular dynamics, *Biochemistry 42*, 562−570.
37. Behrendt, R., Renner, C., Schenk, M., Wang, F. Q., Wachtveitl, J., Oesterhelt, D., and Moroder, L. (1999) Photomodulation of the conformation of cyclic peptides with azobenzene moieties in the peptide backbone, *Angew. Chem., Int. Ed. 38*, 2771−2774.
38. Renner, C., Behrendt, R., Spörlein, S., Wachtveitl, J., and Moroder, L. (2000) Photomodulation of conformational states. I. Mono- and bicyclic peptides with (4-amino)phenylazobenzoic acid as backbone constituent, *Biopolymers 54*, 489−500.
39. Renner, C., Cramer, J., Behrendt, R., and Moroder, L. (2000) Photomodulation of conformational states. II. Mono- and bicyclic peptides with (4-aminomethyl)phenylazobenzoic acid as backbone constituent, *Biopolymers 54*, 501−514.
40. Spörlein, S., Carstens, H., Satzger, H., Renner, C., Behrendt, R., Moroder, L., Tavan, P., Zinth, W., and Wachtveitl, J. (2002) Ultrafast spectroscopy reveals subnanosecond peptide conformational dynamics and validates molecular dynamics simulation, *Proc. Natl. Acad. Sci. U.S.A. 99*, 7998−8002.
41. Bredenbeck, J., Helbing, J., Sieg, A., Schrader, T., Zinth, W., Renner, C., Behrendt, R., Moroder, L., Wachtveitl, J., and Hamm, P. (2003) Picosecond conformational transition and equilibration of a cyclic peptide, *Proc. Natl. Acad. Sci. U.S.A. 100*, 6452−6457.
42. Wachtveitl, J., Sporlein, S., Satzger, H., Fonrobert, B., Renner, C., Behrendt, R., Oesterhelt, D., Moroder, L., and Zinth, W. (2004) Ultrafast conformational dynamics in cyclic azobenzene peptides of increased flexibility, *Biophys. J. 86*, 2350−2362.

43. Carstens, H. (2004) *Doktorarbeit*, Fakultät für Physik, Ludwig-Maximilians-Universität München, Munich, Germany.
44. Bax, A., and Davis, D. G. (1985) MLEV-17 based two-dimensional homonuclear magnetization transfer spectroscopy, *J. Magn. Reson. 65*, 355−360.
45. Bax, A., and Davis, D. G. (1985) Practical aspects of two-dimensional transverse NOE spectroscopy, *J. Magn. Reson. 63*, 207−213.
46. Rance, M., Sorensen, O. W., Bodenhausen, G., Wagner, G., Ernst, R. R., and Wüthrich, K. (1983) Improved spectral resolution in COSY ^{1}H NMR spectra of proteins via double quantum filtering, *Biochem. Biophys. Res. Commun. 117*, 479−485.
47. MacKerell, A. D., Bashford, D., Bellott, M., Dunbrack, R. L., Evanseck, J. D., Field, M. J., Fischer, S., Gao, J., Guo, H., Ha, S., Joseph-McCarthy, D., Kuchnir, L., Kuczera, K., Lau, F. T. K., Mattos, C., Michnick, S., Ngo, T., Nguyen, D. T., Prodhom, B., Reiher, W. E., Roux, B., Schlenkrich, M., Smith, J. C., Stote, R., Straub, J., Watanabe, M., Wiorkiewicz-Kuczera, J., Yin, D., and Karplus, M. (1998) All-atom empirical potential for molecular modeling and dynamics studies of proteins, *J. Phys. Chem. B 102*, 3586−3616.
48. Bordat, P., Sacristan, J., Reith, D., Girard, S., Glattli, A., and Müller-Plathe, F. (2003) An improved dimethyl sulfoxide force field for molecular dynamics simulations, *Chem. Phys. Lett. 374*, 201−205.
49. Mathias, G., Egwolf, B., Nonella, M., and Tavan, P. (2003) A fast multipole method combined with a reaction field for long-range electrostatics in molecular dynamics simulations: The effects of truncation on the properties of water, *J. Chem. Phys. 118*, 10847−10860.
50. Niedermeier, C., and Tavan, P. (1994) A structure adapted multipole method for electrostatic interactions in protein dynamics, *J. Chem. Phys. 101*, 734−748.
51. Eichinger, M., Grubmüller, H., Heller, H., and Tavan, P. (1997) FAMUSAMM: An algorithm for rapid evaluation of electrostatic interactions in molecular dynamics simulations, *J. Comput. Chem. 18*, 1729−1749.
52. Krautler, V., van Gunsteren, W. F., and Hünenberger, P. H. (2001) A fast SHAKE: Algorithm to solve distance constraint equations for small molecules in molecular dynamics simulations, *J. Comput. Chem. 22*, 501−508.
53. Berendsen, H. J. C., Postma, J. P. M., van Gunsteren, W. F., DiNola, A., and Haak, J. R. (1984) Molecular dynamics with coupling to an external bath, *J. Chem. Phys. 81*, 3684−3690.
54. Kloppenburg, M., and Tavan, P. (1997) Deterministic annealing for density estimation by multivariate normal mixtures, *Phys. Rev. E: Stat. Phys., Plasmas, Fluids, Relat. 55*, R2089−R2092.
55. Albrecht, S., Busch, J., Kloppenburg, M., Metze, F., and Tavan, P. (2000) Generalized radial basis function networks for classification and novelty detection: Self-organization of optimal Bayesian decision, *Neural Networks 13*, 1075−1093.
56. Grubmüller, H., and Tavan, P. (1994) Molecular dynamics of conformational substates for a simplified protein model, *J. Chem. Phys. 101*, 5047−5057.
57. Hamprecht, F. A., Peter, C., Daura, X., Thiel, W., and van Gunsteren, W. F. (2001) A strategy for analysis of (molecular) equilibrium simulations: Configuration space density estimation, clustering, and visualization, *J. Chem. Phys. 114*, 2079−2089.
58. Jammalamadaka, S. R., and SenGupta, A. (2001) *Topics in Circular Statistics*, World Scientific Publishing, Singapore.
59. Bürgi, R., Pitera, J., and van Gunsteren, W. F. (2001) Assessing the effect of conformational averaging on the measured values of observables, *J. Biomol. NMR 19*, 305−320.
60. Abseher, R., Horstink, L., Hilbers, C. W., and Nilges, M. (1998) Essential spaces defined by NMR structure ensembles and molecular dynamics simulation show significant overlap, *Proteins 31*, 370−382.
61. Balsera, M. A., Wriggers, W., Oono, Y., and Schulten, K. (1996) Principal component analysis and long time protein dynamics, *J. Phys. Chem. 100*, 2567−2572.
62. Becker, O. M. (1998) Principal coordinate maps of molecular potential energy surfaces, *J. Comput. Chem. 19*, 1255−1267.
63. de Groot, B. L., Daura, X., Mark, A. E., and Grubmüller, H. (2001) Essential dynamics of reversible peptide folding: Memory-free conformational dynamics governed by internal hydrogen bonds, *J. Mol. Biol. 309*, 299−313.
64. Levy, Y., and Becker, O. M. (2001) Energy landscapes of conformationally constrained peptides, *J. Chem. Phys. 114*, 993−1009.
65. Rhee, Y. M., and Pande, V. S. (2003) Multiplexed-replica exchange molecular dynamics method for protein folding simulation, *Biophys. J. 84*, 775−786.
66. Humphrey, W., Dalke, A., and Schulten, K. (1996) VMD−Visual Molecular Dynamics, *J. Mol. Graphics 14*, 33−38.

BI047453R